

# Bi-altermagnetism unveiled by sublattice-specific circular dichroism in resonant inelastic X-ray scattering

G. Channagowdra,<sup>1</sup> A. Singh,<sup>2</sup> H. Y. Huang,<sup>1</sup> M. Furo,<sup>3</sup> Bin Gao,<sup>4,5</sup> Pengcheng Dai,<sup>4,5</sup> C. T. Chen,<sup>1</sup> J. Kuneš,<sup>6</sup> A. Fujimori,<sup>1,7,8</sup> S-W. Cheong,<sup>9</sup> A. Hariki,<sup>3,\*</sup> and D. J. Huang<sup>1,7,10,†</sup>

<sup>1</sup>National Synchrotron Radiation Research Center, Hsinchu 300092, Taiwan

<sup>2</sup>Department of Physics and Astrophysics, University of Delhi, New Delhi 110007, India

<sup>3</sup>Department of Physics and Electronics, Graduate School of Engineering, Osaka Metropolitan University, 1-1 Gakuen-cho, Nakaku, Sakai, Osaka 599-8531, Japan

<sup>4</sup>Department of Physics and Astronomy, Rice University, Houston, 77005 Texas, USA

<sup>5</sup>Rice Laboratory for Emergent Magnetic materials and Smalley-Curl Institute, Rice University, Houston, 77005 Texas, USA

<sup>6</sup>Department of Condensed Matter Physics, Faculty of Science, Masaryk University, Kotlářská 2, 611 37 Brno, Czechia

<sup>7</sup>Department of Physics, National Tsing Hua University, Hsinchu 300044, Taiwan

<sup>8</sup>Department of Physics, University of Tokyo, Bunkyo-Ku, Tokyo 113-0033, Japan

<sup>9</sup>Keck Center for Quantum Magnetism and Department of Physics and Astronomy, Rutgers University, Piscataway, NJ 08854, USA

<sup>10</sup>Department of Electrophysics, National Yang Ming Chiao Tung University, Hsinchu 300093, Taiwan

(Dated: December 2, 2025)

An altermagnet is a recently identified class of magnets that exhibit a zero net magnetic moment but break symmetry under the combined operations of parity and time reversal. It typically consists of two magnetic sites of opposite spins related by rotation within the unit cell. Here, we use circular dichroism (CD) in resonant inelastic X-ray scattering (RIXS) to identify a new form of altermagnetism, namely bi-altermagnetism, in the correlated insulator  $\text{Fe}_2\text{Mo}_3\text{O}_8$ , which comprises two altermagnetic sublattices: one with alternating quasi-octahedral Fe environments and the other with alternating tetrahedral Fe environments. We experimentally revealed the emergence of CD in an achiral, zero-magnetization system, thereby probing mirror-symmetry breaking associated with altermagnetic order. Notably, the CD appeared at sublattice-specific excitations of the octahedral and tetrahedral sites, indicating symmetry breaking in both altermagnetic sublattices. Calculations based on a model with the bi-altermagnetic order along the  $c$  axis successfully reproduce the observed CD. Our findings provide compelling evidence for bi-altermagnetism in  $\text{Fe}_2\text{Mo}_3\text{O}_8$ , and showcase the use of RIXS-CD as a probe of magnetic sublattices in systems with zero net magnetization.

Magnetism, arising from the spin and orbital motion of electrons, is pivotal in condensed matter physics and in a wide range of technological applications. The exchange interactions between electrons determine the spin coupling, resulting in a magnetic long-range order. Recently, a novel magnetic state—altermagnet—has been proposed [1–7], in which atomic moments form a collinear alternating pattern, enabling symmetries that allow typical ferromagnetic behaviors [8–10], while retaining compensated magnetization in the non-relativistic limit. The altermagnetic symmetry gives rise to a number of interesting phenomena such as spin splitting of electronic bands [1–7, 11–17], anomalous Hall effect [5, 13, 18–22], odd magneto-optical effect [23–25], chiral splitting of magnons [26, 27].

Although a growing number of candidate altermagnets have been proposed through theoretical studies based on symmetry [2, 10], only a limited number have been experimentally confirmed [28–34]. This motivates the exploration of materials that preserve the essential features of altermagnetism while introducing new tunability over electronic or crystal structures. Here, we consider  $\text{Fe}_2\text{Mo}_3\text{O}_8$  as a prototypical altermagnet composed of two altermagnetic sublattices that are not related by any crystallographic symmetry.  $\text{Fe}_2\text{Mo}_3\text{O}_8$

is a multiferroic polar compound featuring two inequivalent  $\text{Fe}^{2+}$  sites in quasi-octahedral ( $O_h$ ) and tetrahedral ( $T_d$ ) environments [9, 35–38], as shown in Fig. 1a. It belongs to the point group  $6mm$  in the paramagnetic phase and transitions to the magnetic point group  $6'mm'$  with zero net magnetization in the magnetically ordered phase. In this phase, the mirror symmetries with respect to the three mirror planes are broken by the Néel order with the spin directions along the crystallographic  $c$  axis and are restored only when combined with time reversal  $\mathcal{T}$ ; this combined operation defines the  $m'$  planes shown in Fig. 1b. This symmetry breaking permits both symmetric and antisymmetric spin splittings [39]. As such,  $\text{Fe}_2\text{Mo}_3\text{O}_8$  is predicted to be an A/S-type altermagnet [10]. Notably, from the symmetry perspective, both  $O_h$  and  $T_d$  sublattices in this system can individually support altermagnetic order; therefore, we propose to call  $\text{Fe}_2\text{Mo}_3\text{O}_8$  a “bi-altermagnet.”

Identifying and further characterizing bi-altermagnetism in  $\text{Fe}_2\text{Mo}_3\text{O}_8$  poses several challenges. First, the magnetic (relativistic) symmetry of the Néel state characterized by the Néel vector  $\mathbf{L}||c$  prohibits its manifestation in conventional experimental probes of time-reversal symmetry breaking associated with altermagnetism, such as the anomalous Hall effect and X-ray magnetic circular dichroism (XMCD) in absorption [21, 23]. Second, both magnetic sublattices, octahedral and tetrahedral, may independently exhibit altermagnetism, complicating efforts to determine whether the concept of bi-

\* email: hariki@omu.ac.jp

† email: djhuang@nsrrc.org.tw

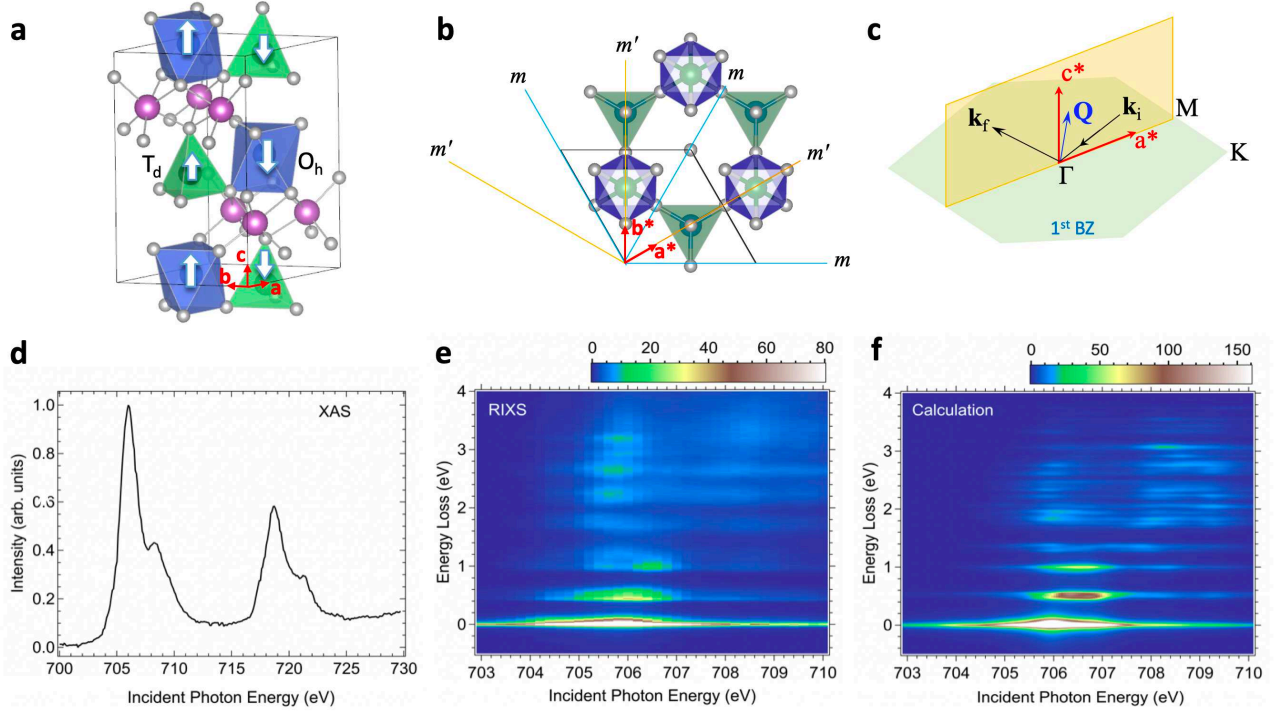


FIG. 1. **Energy-dependent RIXS of  $\text{Fe}_2\text{Mo}_3\text{O}_8$ .** **a**, Crystal structure of  $\text{Fe}_2\text{Mo}_3\text{O}_8$ . The unit cell outlined by a black cuboid contains two quasi-octahedral ( $O_h$ ) and two tetrahedral ( $T_d$ )  $\text{Fe}^{2+}$  sites, whose spin moments are antiparallel, as indicated by the white arrows. **b**, Illustration of the mirror planes in the magnetic point group  $6'mm'$ . Each of the  $O_h$  and  $T_d$  polyhedra in the plane  $z = 0$  form a triangular lattice and both together a hexagonal arrangement. Three vertical mirror planes, indicated by orange lines, correspond to the  $m'$  planes, and the other three, shown in light blue, correspond to the glide planes  $m$ . The reciprocal lattice vectors  $\mathbf{a}^*$  and  $\mathbf{b}^*$  are shown by red arrows. **c**, Illustration of scattering geometry. The scattering plane, defined by the incident wave vector  $\mathbf{k}_i$  and the scattered wave vector  $\mathbf{k}_f$ , lies in the  $\mathbf{a}^*\mathbf{c}^*$  plane, i.e., one of the  $m'$  planes. The momentum transfer is given by  $\mathbf{Q} = \mathbf{k}_f - \mathbf{k}_i$ . The light blue hexagon indicates the first Brillouin zone (BZ) of the reciprocal lattice. **d**, Fe  $L$ -edge XAS spectrum measured in the fluorescence yield mode. The XAS is plotted without corrections for self-absorption. **e**, RIXS intensity map plotted in the plane of energy loss vs. incident photon energy. Data were measured by using right-handed circularly polarized (RCP) X-rays at 32 K for incident photon energy across the  $L_3$  peak of XAS. **f**, Corresponding theoretical RIXS intensity map.

altomagnetism is applicable to this material. For example, while direct observation of spin splitting in the band structure via angle-resolved photoemission spectroscopy could positively identify altomagnetism, it does not allow disentangling the contributions of the interpenetrating sublattices.

In this Article, we propose and apply a method based on site-selective resonant inelastic X-ray scattering (RIXS) with circularly polarized lights to identify and characterize bi-altomagnetism in  $\text{Fe}_2\text{Mo}_3\text{O}_8$ . At the Fe  $L$ -edge, RIXS promotes a  $2p$  core electron to the Fe  $3d$  shell, followed by the decay of a  $3d$  electron to the core level with X-ray emission. This coherent process creates a charge-neutral excitation, which may either propagate through the lattice or remain localized at the excited site. The former corresponds to collective excitations such as magnons, while the latter involves intra-atomic excitations, including spin-flip and crystal-field transitions, whose energies depend on the magnetic site and thus provide sensitivity to individual sublattices. We reveal clear circular dichroism (CD) in these sublattice-specific excitations. The temperature dependence of the CD, together with theoretical simulations considering the bi-altomagnetic order,

supports the realization of bi-altomagnetism in  $\text{Fe}_2\text{Mo}_3\text{O}_8$ .

## RESULTS AND DISCUSSION

### RIXS of $\text{Fe}_2\text{Mo}_3\text{O}_8$

We measured RIXS with the incident photon energy tuned across the Fe  $L_3$  edge. Figure 1d depicts the X-ray absorption spectrum (XAS) of  $\text{Fe}_2\text{Mo}_3\text{O}_8$  at the Fe  $L$  edge, while Fig. 1e shows the RIXS intensity map plotted in the plane of energy loss versus incident photon energy. The energy levels of the  $3d$  states are reversed at the two  $\text{Fe}^{2+}$  sites with  $O_h$  and  $T_d$  symmetries. Previous density functional theory (DFT) studies [37, 38], as well as our theoretical analysis presented in the Supplementary Information, show that the tetrahedral and octahedral sites have quite different crystal-field splittings, of about 0.5 eV and 1.0 eV, respectively. This difference allows us to identify site-resolved excitations in RIXS, as demonstrated in the theoretical RIXS intensity map shown in Fig. 1f and the discussions below. Our RIXS data show that the resonance energy window of the  $e \rightarrow t_2$  excitations ( $\sim 0.5$  eV) at the  $T_d$  sites is significantly broader and occurs at lower incident photon energy than that of the  $t_{2g} \rightarrow e_g$  excitations

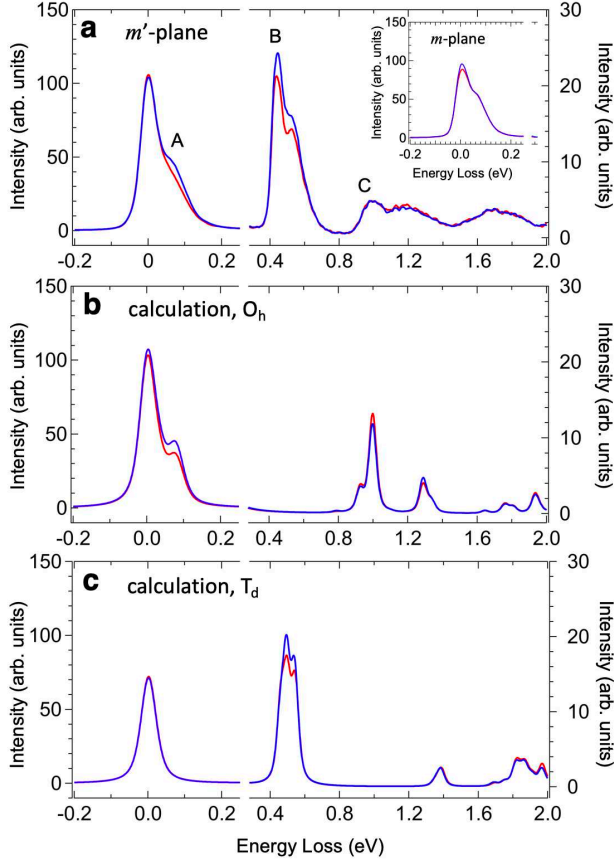


FIG. 2. **CD in RIXS of  $\text{Fe}_2\text{Mo}_3\text{O}_8$ .** **a**, RIXS spectra measured with circularly polarized X-rays and with the scattering plane in the  $\mathbf{a}^*\mathbf{c}^*$  plane ( $m'$  plane) at 32 K, below the Néel temperature  $T_N = 60$  K. Red and blue curves, denoted by RCP and LCP, represent RIXS spectra excited with right- and left-handed circularly polarized incident X-rays, respectively. The RIXS data were recorded with momentum transfer  $\mathbf{Q} = (0.05, 0, 0.65)$ . In the RIXS spectra plotted in **a**, A indicates the low-energy spin-orbital excitations below 0.1 eV, predominantly originating from the  $O_h$  site; B and C label the characteristic features of the crystal-field excitations around 0.5 eV and 1 eV at the  $T_d$  and  $O_h$  sites, respectively. Inset: Corresponding low-energy RIXS spectra with the scattering plane in the  $ac$  plane ( $m$  glide symmetry plane). **b**, **c**, Calculations for the quasi  $O_h$  and  $T_d$  sites, where the contributions from the two magnetic sublattices (up- and down-spin) are summed.

( $\sim 1$  eV) at the  $O_h$  sites. This site assignment is corroborated by the theoretical simulation shown in Fig. 1f. As discussed later, we also observe spin-orbital excitations below 0.1 eV (labeled A in Fig. 2a), originating from transitions within the  $t_{2g}$  manifold of the  $\text{Fe}^{2+}$  ion at the  $O_h$  site, with resonance energies lower than those of the crystal-field excitations.

Figure 2a shows the RIXS spectra of  $\text{Fe}_2\text{Mo}_3\text{O}_8$  with an incident photon energy tuned to the  $L_3$  XAS peak (706 eV) at momentum transfer  $\mathbf{Q} = (0.05, 0, 0.65)$  in reciprocal lattice units, with which all momentum transfers are expressed throughout the Article. The spectra exhibit characteristic features labeled A, B, and C, which are well separated in energy. These features exhibit distinct Fe-site character. Feature B is

assigned to transitions between the  $e$  and  $t_2$  states at the  $T_d$  site, while feature C corresponds to transitions between the  $t_{2g}$  and  $e_g$  states at the  $O_h$  site. Around the energy of feature C, additional multiplet excitations ( $^3T_1$ ,  $^1A_1$ ) are present. These, however, have weaker RIXS intensities and originate exclusively from the octahedral site, as demonstrated by our multiplet analysis in the Supplementary Information. Furthermore, feature A represents an excitation at the octahedral site. We define feature A as the broad structure centered at about 70 meV that exhibits CD. It is attributed to spin-orbital excitations at the  $O_h$  site, with negligible contribution from the tetrahedral site, since the spin-orbital excitation at the tetrahedral site lies well below 50 meV (see Fig. S6(a,e) in the Supplementary Information) and does not yield significant CD, as discussed below.

### CD in RIXS and bi-altermagnetism

Given the site resolution provided by the RIXS technique, we proceed to confirm the bi-altermagnetism of  $\text{Fe}_2\text{Mo}_3\text{O}_8$  through the circular polarization profile and the temperature dependence of the site-specific excitations at the  $T_d$  and  $O_h$  sites revealed above. However, care must be taken in choosing the experimental geometry to ensure that the CD remains sensitive to altermagnetism, as CD in RIXS is not inherently sensitive to time-reversal symmetry breaking [40, 41]. This originates from the non-Hermiticity inherent in the coherent RIXS process, encoded in the  $i\Gamma$  term of the propagator in the Kramers–Heisenberg formula,  $\sum_m |m\rangle \langle m| / (\omega_{\text{in}} + E_i - E_m + i\Gamma)$ , where  $|m\rangle$ ,  $\omega_{\text{in}}$ ,  $E_i$ ,  $E_m$ , and  $\Gamma$  denote, respectively, the intermediate eigenstate, the energy of the incident X-rays, the energies of the initial and intermediate states, and the core-hole lifetime broadening. This prevents mapping of the RIXS intensities between the  $\mathbf{L}$  and  $-\mathbf{L}$  states by the time-reversal  $\mathcal{T}$ , and thus  $\mathcal{T}$  alone cannot enforce the vanishing of CD, in principle allowing CD even in the paramagnetic phase [41]. Therefore, RIXS-CD reflects only the unitary symmetries and their changes across phase transitions. This consideration motivates us to employ a RIXS geometry with the scattering plane in the  $m'$  plane, as illustrated in Fig. 1c, where the mirror-symmetry operation maps the left- and right-circularly polarized incident X-rays onto each other and enforces the absence of CD in the paramagnetic phase. This mirror symmetry is broken by the altermagnetic order with the Néel vector (pseudovector) along the  $c$  axis, allowing CD to emerge below the transition temperature.

For this geometry with the  $m'$  plane, we observed clear CD for both features A and B in the altermagnetic ordered phase at  $T = 32$  K, below the Néel temperature  $T_N = 60$  K, as shown in Fig. 2a. Figures 3a–3h show the temperature dependence of the RIXS CD. As the temperature increased above  $T_N$ , the CD vanished within the experimental uncertainty. This temperature evolution establishes a direct link between the observed CD and the underlying altermagnetic order. In contrast, previous RIXS-CD studies on  $\alpha\text{-MnTe}$  [40, 42] and  $\text{CrSb}$  [43] have not revealed such a disappearance, as their high Néel temperatures preclude access to the paramagnetic phase above  $T_N$ . To further verify the relation between CD in RIXS and symmetry breaking, we also measured CD for the scattering

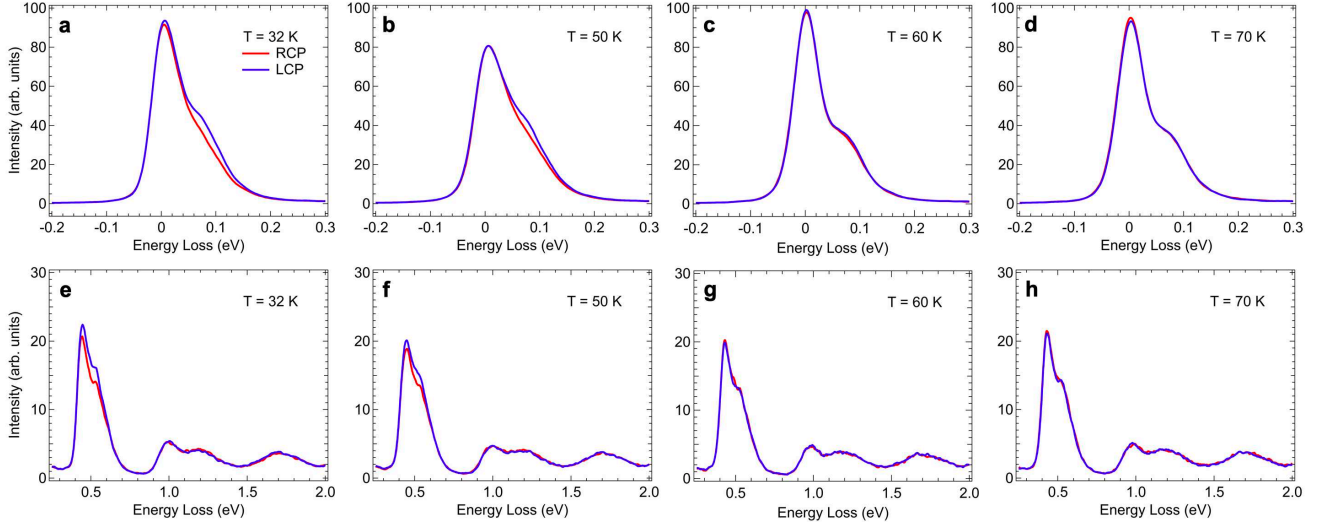


FIG. 3. **Temperature-dependent circular dichroism (CD) in RIXS of  $\text{Fe}_2\text{Mo}_3\text{O}_8$ .** **a-d**, CD in RIXS arising from spin-orbital excitations near 0.1 eV. **e-h**, CD in RIXS arising from  $dd$  excitations. The spectra were measured at momentum transfer  $\mathbf{Q} = (0.03, 0, 0.66)$  using circularly polarized X-rays at selected temperatures across the Néel temperature  $T_N = 60$  K. Red and blue curves (RCP and LCP) correspond to spectra excited with right- and left-handed circularly polarized incident X-rays, respectively. Additional RIXS-CD data at other temperatures are shown in Figs. S2 and S3 of the Supplementary Information.

plane in the  $m$  plane shown in Fig. 1b. This mirror (glide) plane is preserved even in the altermagnetic phase, which forbids CD. Indeed, the CD for this geometry vanishes within the present experimental accuracy; see the inset of Fig. 2a and Fig. S1 in the Supplementary Information for detailed comparisons. This supports the conclusion that the appearance of CD in the  $m'$ -plane geometry reflects its symmetry breaking associated with the magnetic order.

To support the bi-altermagnetic origin of the observed CD and to examine their character, we performed simulations using two  $\text{Fe}^{2+}$  ionic models with quasi-octahedral and tetrahedral crystal fields. The parameters were derived from first-principles calculations and further refined to reproduce the energy positions of the  $dd$  features in the present RIXS spectra (see Supplementary Information for details). To simulate the altermagnetic order ( $\mathbf{L}||c$ ), we introduce a staggered Weiss (molecular) field acting on the two magnetic sublattices within each unit, with the total contribution obtained by summing over the sublattices [23, 41]. The simulations shown in Figs. 2b and 2c for both Fe sites in the altermagnetic phase reproduce the experimentally observed CD below  $T_N$ . The CD vanishes in the paramagnetic phase (not shown) as required by symmetry. This supports the interpretation that changes in the CD of features A and B reflect symmetry changes at both sites associated with the onset of altermagnetic order. In the models used, all excitations are confined to the excited site, and direct interactions, such as the hopping of  $3d$  electron, between the Fe sites are not taken into account. The agreement with the experimental data therefore demonstrates that the excitations exhibit a localized character and that the presence of CD directly indicates broken symmetry in the excitation spectrum at both octahedral and tetrahedral sites, confirming the realization of bi-altermagnetism in the system.

Note that feature C, which originates predominantly from crystal-field ( ${}^5E$ ) and partly multiplet excitations ( ${}^3T_1$ ) at the octahedral sites (see Fig. S5 in the Supplementary Information), exhibits negligible CD signals in the experimental data. This behavior is not implied by symmetry, but stems from large lifetime broadening and the character of the corresponding wave functions.

We remark on the RIXS-CD in comparison to other probes. CD in X-ray absorption of achiral systems without net magnetization usually vanishes. Indeed, the magnetic symmetry of  $\text{Fe}_2\text{Mo}_3\text{O}_8$  forbids XMCD. This can be seen from the presence of three mirror (glide) planes  $m$ , which prohibits XMCD and also anomalous Hall effect by symmetry. Furthermore, these responses generally do not have sublattice resolution. In contrast, CD in RIXS obeys different symmetry constraints and can be finite even in such a compensated magnet, as mentioned above. Moreover, CD in RIXS can be attributed to individual sublattices, as dichroic contributions at different energies are not subject to mutual cancellation once allowed at each sublattice. The observed sublattice CD is sizable and can be analyzed by a simple model. Therefore, RIXS-CD offers a new opportunity to study magnetic sublattices in such complex altermagnetic systems, and, more broadly, in antiferromagnetic systems.

### Spin-orbital excitations

The magnons seen at low energies are in general dispersive excitations and shall exhibit some chiral splitting [26, 27]. However, the dispersion observed within the studied momentum range is small (see Fig. S4 in the Supplementary Information), and the present RIXS resolution is not sufficient to resolve such splitting. A dispersion in the very low-energy region (10-15 meV) has been reported by neutron scatter-



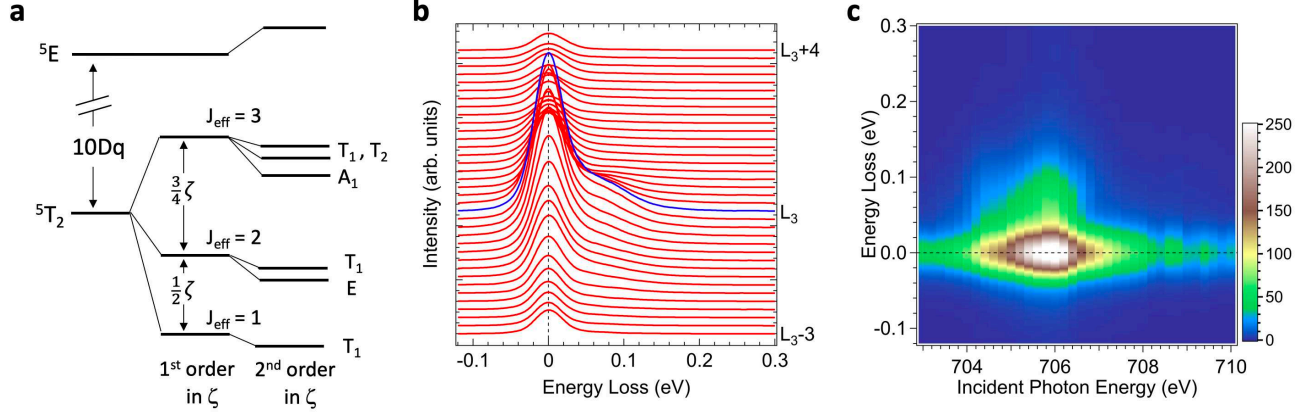


FIG. 4. **Spin-orbital excitations of  $\text{Fe}_2\text{Mo}_3\text{O}_8$  probed by RIXS.** **a**, Energy level diagram of  $\text{Fe}^{2+}$  in an octahedral crystal field with spin-orbit coupling in first- and second-order approximations. For an atomic SOC constant  $\zeta = 52$  meV, atomic multiplet calculations show that the energies of the quintet substates ( $E$  and  $T_1$ ) are 23.7 and 25.6 meV, and those of the septet substates ( $A_1$ ,  $T_1$ , and  $T_2$ ) are 58.1, 62.1, and 64.8 meV. **b**, Energy-dependent RIXS measured at  $T = 32$  K with RCP. **c**, Corresponding RIXS intensity map.

ing [44], but this technique is typically not suitable for detecting higher-energy excitation energy, where we observed a CD signal that is well reproduced by the atomic/impurity model. This suggests that the observed CD arises predominantly from the wave-vector dependence of the polarization (dipole) operators rather than momentum dependence of the final-state wave functions.

Finally, we discuss the possible spin- and orbital-entangled nature of the low-energy excitations and the ground state of  $\text{Fe}_2\text{Mo}_3\text{O}_8$ , within the ionic  $\text{Fe}^{2+}$  model picture. The divalent Fe at the quasi-octahedral site adopts the  $5T_2$  ground-state multiplet, which hosts active spin and orbital degrees of freedom in the absence of spin-orbit coupling (SOC) within the Fe  $3d$  shell [45]. SOC splits the  $5T_2$  state into triplet, quintet, and septet states with effective angular momentum  $J_{\text{eff}} = 1, 2$ , and  $3$  (the lowest  $J_{\text{eff}} = 1$  state being  $T_{1g}$ ), as illustrated in Fig. 4a [46]. For an atomic SOC constant  $\zeta$ , the energy separations between  $J_{\text{eff}} = 1$  and  $2$ , and between  $2$  and  $3$ , are approximately  $\zeta/2$  and  $3\zeta/4$ , respectively, in the first-order approximation (see the Supplementary Information). In the second-order approximation, the  $J_{\text{eff}} = 2$  and  $3$  states are further split into substates. Figures 4b and 4c present the low-energy RIXS spectra and corresponding intensity map as functions of incident photon energy, revealing spin-orbital excitations within the  $5T_2$  manifold. We fit the low-energy spectra with two components corresponding to transitions from the ground-state triplet to the quintet and septet states, and found that their energy ratio is close to 2:3—consistent with the prediction of the zero-order approximation (see Fig. S4). Together with the simulation of RIXS presented in the Supplementary Information, which shows only a marginal role of the trigonal distortion effect, our result indicates that the low-energy excitations exhibit spin-orbit  $J_{\text{eff}}$  character.

The tetrahedral site, adopting the  $5E$  ground state, does not yield significant splitting by SOC, and its excitation remains well below 50 meV in the altermagnetically ordered phase, which has allowed us to attribute feature A predominantly

to the octahedral site. While SOC leads to a singlet ground state  $A_1$ , the Weiss (exchange) field in the ordered phase generates a large magnetic moment, indicating Van Vleck-type magnetism at the  $T_d$  site. Moreover, the ground state possesses not only spin but also orbital angular momentum, owing to the active orbital degrees of freedom, with the orbital contribution amounting to about 20% of the spin moment in the ionic model employed (see Supplementary Information for details). The conventional concept of altermagnetism rests on the non-relativistic limit, where spin and orbital degrees of freedom are decoupled. Furthermore, in many transition-metal compounds, the orbital moments are often quenched in the low-energy manifold, as in established altermagnets such as  $\alpha\text{-MnTe}$  and  $\text{CrSb}$ . Our result highlights  $\text{Fe}_2\text{Mo}_3\text{O}_8$  as a rare example among transition-metal altermagnets that retain active orbital magnetism.

## METHODS

### $\text{Fe}_2\text{Mo}_3\text{O}_8$ crystal growth

Single crystals of  $\text{Fe}_2\text{Mo}_3\text{O}_8$  were synthesized using a two-step method [35]. First, polycrystalline  $\text{Fe}_2\text{Mo}_3\text{O}_8$  was prepared by a conventional solid-state reaction. Stoichiometric amounts of  $\text{Fe}_2\text{O}_3$ , Mo, and  $\text{MoO}_3$  powders were thoroughly ground, pelletized, and sealed in evacuated quartz tubes. The mixture was reacted at high temperature to yield phase-pure polycrystalline material. In the second step, single crystals were grown via chemical vapor transport (CVT) using  $\text{TeCl}_4$  as the transport agent. The polycrystalline powder and a measured amount of  $\text{TeCl}_4$  were sealed together in an evacuated silica ampoule and placed in a two-zone furnace, where the source and growth zones were maintained at  $958^\circ\text{C}$  and  $853^\circ\text{C}$ , respectively, for about 10 days. The temperature gradient promoted directional transport of volatile species, resulting in the growth of shiny black hexagonal crystals. The resulting crystals were easily detached from the tube walls and cleaned with dilute hydrochloric acid without signs of surface

oxidation.

The crystallinity and phase purity of the as-grown  $\text{Fe}_2\text{Mo}_3\text{O}_8$  crystals were first confirmed by powder X-ray diffraction (XRD) performed on ground single crystals. The diffraction pattern matched well with the reported pattern for  $\text{Fe}_2\text{Mo}_3\text{O}_8$ , with no detectable impurity phases. Room-temperature refinement of the XRD data yielded a hexagonal unit cell with lattice parameters  $a = 5.773(3) \text{ \AA}$  and  $c = 10.054(3) \text{ \AA}$ , consistent with previous reports [47]. The crystal structure was indexed in the polar space group  $P6_3mc$ . Back-reflection Laue X-ray diffraction was used to verify the single crystallinity and to orient the crystals for subsequent measurements. These characterizations confirm that the grown samples are phase-pure and structurally well-ordered, suitable for further spectroscopic and scattering studies.

### RIXS measurements

We conducted Fe  $L_3$ -edge RIXS measurements on  $\text{Fe}_2\text{Mo}_3\text{O}_8$  single crystals at beamline 41A of the Taiwan Photon Source [48]. The RIXS scattering plane was defined by the [100] and [001] directions in the reciprocal space. The incident X-ray polarization was switchable between linear and circular modes. Prior to RIXS measurements, we determined the incident X-ray energy by measuring X-ray absorption spectra recorded in the fluorescence-yield mode using a photodiode. The total energy resolution of RIXS, including contributions from both the monochromator and the spectrometer, was 45 meV with a full width at half maximum.

### Theoretical calculations

We simulate the RIXS intensities using  $\text{Fe}^{2+}$  ( $d^6$ ) ionic models. This approach is widely used to describe localized  $dd$  excitations in RIXS spectra of correlated insulators, including crystal-field and Coulomb multiplet excitations. The model Hamiltonian includes (i) valence–valence interactions within the  $3d$  shell, (ii) core–valence interactions between the  $3d$  and  $2p$  shells in the intermediate state of the coherent RIXS process, (iii) spin–orbit coupling in both the  $3d$  and  $2p$  shells, (iv) the crystal-field splitting of the  $3d$  levels, and (v) a staggered Zeeman field applied to the two magnetic sublattices within each  $O_h$  and  $T_d$  site to simulate the altermagnetic ordered phase. The crystal-field terms distinguish the  $O_h$  and  $T_d$  sites, whereas the other interactions are set to common values for both. This construction results in four atomic sites in total (up- and down-spin for both  $O_h$  and  $T_d$ ), and the site contributions are summed following Refs. 23 and 41.

The Hamiltonian is diagonalized numerically to obtain the full eigenvalue spectrum of the initial, intermediate, and final states, and the RIXS intensities are evaluated using the Kramers–Heisenberg formula, with an inverse lifetime broadening fixed at  $\Gamma = 0.3 \text{ eV}$ . The crystal-field parameters are derived from DFT calculations using the Wien2k and Wanner90 packages [49, 50], based on the experimental crystal structures, yielding results consistent with previous DFT studies [37, 38]. The Slater integrals for the  $2p$ – $3d$  interac-

tion are obtained from atomic Hartree–Fock calculations and reduced to 70% of their atomic values to account for the effects of higher configurations neglected in the atomic treatment, a well-established procedure for simulating core-level spectra at  $3d$  transition-metal edges. The valence–valence ( $3d$ – $3d$ ) interaction is parameterized by the Hund’s coupling  $J = (F_2 + F_4)/14$ , which is set to 0.75 eV, a typical value for Fe-based oxides. These parameters are optimized based on the energy positions of the  $dd$  features observed in the present RIXS data. The detailed procedure is provided in the Supplementary Information.

### Acknowledgements

We thank the staff of the Taiwan Photon Source for technical support, and Andrei Sirenko and Hakuto Suzuki for discussions. This work was supported in part by the Taiwan National Science and Technology Council under Grant Nos. NSTC112-2112-M-007-031 and NSTC113-2112-M-007-033. A.S. was partially supported by ANRF (SERB) under grant number 2023/000242. We are also grateful for support from the Japan Society for the Promotion of Science under Grant No. JP22K03535. A.F. acknowledges support from the Yushan Fellow Program of the Ministry of Education (MOE) of Taiwan. This work was also supported by JSPS KAKENHI Grant Numbers 25K00961, 25K07211, 23H03816, 23H03817, the 2025 Osaka Metropolitan University (OMU) Strategic Research Promotion Project (Young Researcher) (A.H.), by the project Quantum materials for applications in sustainable technologies (QM4ST), funded as project No. CZ.02.01.01/00/22 008/0004572 by Programme Johannes Amos Comenius, call Excellent Research, and by the Ministry of Education, Youth and Sports of the Czech Republic through the e-INFRA CZ (ID:90254) (J.K.). Part of the computations in this work were performed using the facilities of the Supercomputer Center, the Institute for Solid State Physics, the University of Tokyo. The single-crystal synthesis efforts at Rice were supported by the U.S. DOE, BES under Grant No. DE-SC0012311 and DE-SC0026179 (P.D.). Part of the materials characterization efforts at Rice was supported by the Robert A. Welch Foundation Grant No. C-1839 (P.D.).

### Author contributions

D.J.H. initiated the project and led the RIXS experiments. A.H. led the theoretical calculations. S.W.C. guided the symmetry discussion. G.C., A.S., H.Y.H., D.J.H., A.F., and C.T.C. conducted the RIXS measurements. B.G. and P.D. synthesized and characterized the samples. G.C., A.S., and D.J.H. analyzed the RIXS data and prepared the experimental figures. M.F., A.H., and J.K. performed the theoretical calculations. D.J.H., A.H., and A.F. wrote the manuscript with input from the other authors.

### Data availability

The data supporting the findings of this study are available from the corresponding authors upon reasonable request.

- 
- [1] L. Šmejkal, J. Sinova, and T. Jungwirth, Beyond Conventional Ferromagnetism and Antiferromagnetism: A Phase with Non-relativistic Spin and Crystal Rotation Symmetry, *Phys. Rev. X* **12**, 031042 (2022).
- [2] L. Šmejkal, J. Sinova, and T. Jungwirth, Emerging Research Landscape of Altermagnetism, *Phys. Rev. X* **12**, 040501 (2022).
- [3] K.-H. Ahn, A. Hariki, K.-W. Lee, and J. Kuneš, Antiferromagnetism in RuO<sub>2</sub> as *d*-wave pomeranchuk instability, *Phys. Rev. B* **99**, 184432 (2019).
- [4] M. Naka, S. Hayami, H. Kusunose, Y. Yanagi, Y. Motome, and H. Seo, Spin current generation in organic antiferromagnets, *Nat. Commun.* **10**, 4305 (2019).
- [5] L. Šmejkal, R. González-Hernández, T. Jungwirth, and J. Sinova, Crystal time-reversal symmetry breaking and spontaneous Hall effect in collinear antiferromagnets, *Sci. Adv.* **6** (2020).
- [6] S. Hayami, Y. Yanagi, and H. Kusunose, Momentum-dependent spin splitting by collinear antiferromagnetic ordering, *J. Phys. Soc. Jpn.* **88**, 123702 (2019).
- [7] L.-D. Yuan, Z. Wang, J.-W. Luo, E. I. Rashba, and A. Zunger, Giant momentum-dependent spin splitting in centrosymmetric low-Z antiferromagnets, *Phys. Rev. B* **102**, 014422 (2020).
- [8] R. Tamang, S. Gurung, D. P. Rai, S. Brahimi, and S. Lounis, Newly discovered magnetic phase: A brief review on altermagnets, *arXiv:2412.05377* (2024).
- [9] Y. Chang, Y. Weng, Y. Xie, B. You, J. Wang, L. Li, J.-M. Liu, S. Dong, and C. Lu, Colossal linear magnetoelectricity in polar magnet Fe<sub>2</sub>Mo<sub>3</sub>O<sub>8</sub>, *Phys. Rev. Lett.* **131**, 136701 (2023).
- [10] S.-W. Cheong and F.-T. Huang, Altermagnetism classification, *npj Quantum Mater.* **10**, 38 (2025).
- [11] S. Hayami, Y. Yanagi, and H. Kusunose, Bottom-up design of spin-split and reshaped electronic band structures in antiferromagnets without spin-orbit coupling: Procedure on the basis of augmented multipoles, *Phys. Rev. B* **102**, 144441 (2020).
- [12] L.-D. Yuan, Z. Wang, J.-W. Luo, and A. Zunger, Prediction of low-Z collinear and noncollinear antiferromagnetic compounds having momentum-dependent spin splitting even without spin-orbit coupling, *Phys. Rev. Mater.* **5**, 014409 (2021).
- [13] I. I. Mazin, K. Koepf, M. D. Johannes, R. González-Hernández, and L. Šmejkal, Prediction of unconventional magnetism in doped FeSb<sub>2</sub>, *Proc. Natl. Acad. Sci. U.S.A.* **118**, e2108924118 (2021).
- [14] P. Liu, J. Li, J. Han, X. Wan, and Q. Liu, Spin-Group Symmetry in Magnetic Materials with Negligible Spin-Orbit Coupling, *Phys. Rev. X* **12**, 021016 (2022).
- [15] J. Yang, Z.-X. Liu, and C. Fang, Symmetry invariants and classes of quasiparticles in magnetically ordered systems having weak spin-orbit coupling, *Nat. Commun.* **15**, 10203 (2024).
- [16] L.-D. Yuan, A. B. Georgescu, and J. M. Rondinelli, Nonrelativistic spin splitting at the Brillouin zone center in compensated magnets, *Phys. Rev. Lett.* **133**, 216701 (2024).
- [17] R. M. Fernandes, V. S. De Carvalho, T. Birol, and R. G. Pereira, Topological transition from nodal to nodeless Zeeman splitting in altermagnets, *Phys. Rev. B* **109**, 024404 (2024).
- [18] M. Naka, S. Hayami, H. Kusunose, Y. Yanagi, Y. Motome, and H. Seo, Anomalous hall effect in  $\kappa$ -type organic antiferromagnets, *Phys. Rev. B* **102**, 075112 (2020).
- [19] L. Šmejkal, A. H. MacDonald, J. Sinova, S. Nakatsuji, and T. Jungwirth, Anomalous Hall antiferromagnets, *Nat. Rev. Mater.* **7**, 482 (2022).
- [20] S. Hayami and H. Kusunose, Essential role of the anisotropic magnetic dipole in the anomalous Hall effect, *Phys. Rev. B* **103**, L180407 (2021).
- [21] R. D. Gonzalez Betancourt, J. Zubáč, R. Gonzalez-Hernandez, K. Geishendorf, Z. Šobán, G. Springholz, K. Olejník, L. Šmejkal, J. Sinova, T. Jungwirth, S. T. B. Goennenwein, A. Thomas, H. Reichlová, J. Železný, and D. Krieger, Spontaneous Anomalous Hall Effect Arising from an Unconventional Compensated Magnetic Phase in a Semiconductor, *Phys. Rev. Lett.* **130**, 036702 (2023).
- [22] M. Naka, Y. Motome, and H. Seo, Anomalous Hall effect in antiferromagnetic perovskites, *Phys. Rev. B* **106**, 195149 (2022).
- [23] A. Hariki, A. Dal Din, O. J. Amin, T. Yamaguchi, A. Badura, D. Krieger, K. W. Edmonds, R. P. Campion, P. Wadley, D. Backes, L. S. I. Veiga, S. S. Dhesi, G. Springholz, L. Šmejkal, K. Výborný, T. Jungwirth, and J. Kuneš, X-Ray Magnetic Circular Dichroism in Altermagnetic  $\alpha$ -MnTe, *Phys. Rev. Lett.* **132**, 176701 (2024).
- [24] N. Sasabe, M. Mizumaki, T. Uozumi, and Y. Yamasaki, Ferroic Order for Anisotropic Magnetic Dipole Term in Collinear Antiferromagnets of  $(t_{2g})^4$  System, *Phys. Rev. Lett.* **131**, 216501 (2023).
- [25] X. Zhou, W. Feng, X. Yang, G.-Y. Guo, and Y. Yao, Crystal chirality magneto-optical effects in collinear antiferromagnets, *Phys. Rev. B* **104**, 024401 (2021).
- [26] L. Šmejkal, A. Marmodoro, K.-H. Ahn, R. González-Hernández, I. Turek, S. Mankovsky, H. Ebert, S. W. D'Souza, O. c. v. Šipr, J. Sinova, and T. c. v. Jungwirth, Chiral magnons in altermagnetic RuO<sub>2</sub>, *Phys. Rev. Lett.* **131**, 256703 (2023).
- [27] Z. Liu, M. Ozeki, S. Asai, S. Itoh, and T. Masuda, Chiral split magnon in altermagnetic MnTe, *Phys. Rev. Lett.* **133**, 156702 (2024).
- [28] J. Krempaský, L. Šmejkal, S. W. D'souza, M. Hajlaoui, G. Springholz, K. Uhlířová, F. Alarab, P. C. Constantinou, V. Strocov, D. Usanov, W. R. Pudelko, R. González-Hernández, A. B. Hellenes, Z. Jansa, H. Reichlová, Z. Šobán, R. D. Gonzalez Betancourt, P. Wadley, D. Sinova, J. and Krieger, J. Minár, J. H. Dil, and T. Jungwirth, Altermagnetic lifting of Kramers spin degeneracy, *Nature* **626**, 517 (2024).
- [29] S. Lee, S. Lee, S. Jung, J. Jung, D. Kim, Y. Lee, B. Seok, J. Kim, B. G. Park, L. Šmejkal, C.-J. Kang, and C. Kim, Broken kramers degeneracy in altermagnetic MnTe, *Phys. Rev. Lett.* **132**, 036702 (2024).
- [30] T. Osumi, S. Souma, T. Aoyama, K. Yamauchi, A. Honma, K. Nakayama, T. Takahashi, K. Ohgushi, and T. Sato, Observation of a giant band splitting in altermagnetic MnTe, *Phys. Rev. B* **109**, 115102 (2024).
- [31] S. Reimers, L. Odenbreit, L. Šmejkal, V. N. Strocov, P. Constantinou, A. B. Hellenes, R. Jaeschke Ubierto, W. H. Campos, V. K. Bharadwaj, A. Chakraborty, T. Denneulin, W. Shi, R. E. Dunin-Borkowski, S. Das, M. Kläui, J. Sinova, and M. Jourdan, Direct observation of altermagnetic band splitting in CrSb thin films, *Nat. Commun.* **15**, 2116 (2024).
- [32] J. Ding, Z. Jiang, X. Chen, Z. Tao, Z. Liu, T. Li, J. Liu, J. Sun, J. Cheng, J. Liu, Y. Yang, R. Zhang, L. Deng, W. Jing, Y. Huang, Y. Shi, M. Ye, S. Qiao, Y. Wang, Y. Guo, D. Feng, and D. Shen, Large Band Splitting in *g*-Wave Altermagnet CrSb, *Phys. Rev. Lett.* **133**, 206401 (2024).
- [33] G. Yang, Z. Li, S. Yang, J. Li, H. Zheng, W. Zhu, Z. Pan, Y. Xu, S. Cao, W. Zhao, *et al.*, Three-dimensional mapping of the altermagnetic spin splitting in CrSb, *Nat. Commun.* **16**, 1442 (2025).

- [34] R. Takagi, R. Hirakida, Y. Settai, R. Oiwa, H. Takagi, A. Kitaori, K. Yamauchi, H. Inoue, J.-i. Yamaura, D. Nishio-Hamane, S. Itoh, S. Aji, H. Saito, T. Nakajima, T. Nomoto, R. Arita, and S. Seki, Spontaneous Hall effect induced by collinear antiferromagnetic order at room temperature, *Nat. Mater.* **24**, 63 (2025).
- [35] Y. Wang, G. L. Pascut, B. Gao, T. A. Tyson, K. Haule, V. Kiryukhin, and S.-W. Cheong, Unveiling hidden ferromagnetism and giant magnetoelectricity in polar magnet  $\text{Fe}_2\text{Mo}_3\text{O}_8$ , *Sci. Rep.* **5**, 12268 (2015).
- [36] T. Kurumaji, S. Ishiwata, and Y. Tokura, Doping-tunable ferromagnetic phase with large linear magnetoelectric effect in a polar magnet  $\text{Fe}_2\text{Mo}_3\text{O}_8$ , *Phys. Rev. X* **5**, 031034 (2015).
- [37] S. Reschke, A. A. Tsirlin, N. Khan, L. Prodan, V. Tsurkan, I. Kézsmárki, and J. Deisenhofer, Structure, phonons, and orbital degrees of freedom in  $\text{Fe}_2\text{Mo}_3\text{O}_8$ , *Phys. Rev. B* **102**, 094307 (2020).
- [38] I. Solov'yev and S. Streltsov, Microscopic toy model for magnetoelectric effect in polar  $\text{Fe}_2\text{Mo}_3\text{O}_8$ , *Phys. Rev. Mater.* **3**, 114402 (2019).
- [39] S.-W. Cheong and F.-T. Huang, Trompe L'oeil Ferromagnetism—magnetic point group analysis, *npj Quantum Mater.* **8**, 73 (2023).
- [40] D. Takegami, T. Aoyama, T. Okauchi, T. Yamaguchi, S. Tipireddy, S. Agrestini, M. García-Fernández, T. Mizokawa, K. Ohgushi, K.-J. Zhou, J. Chaloupka, J. Kuneš, A. Hariki, and H. Suzuki, Circular Dichroism in Resonant Inelastic X-ray Scattering: Probing Altermagnetic Domains in MnTe, arXiv:2502.10809 (2025).
- [41] M. Furo, A. Hariki, and J. Kuneš, Theory of circular dichroism in resonant inelastic x-ray scattering, arXiv preprint arXiv:2508.04388 (2025).
- [42] D. Jost, R. B. Regmi, S. Sahel-Schackis, M. Scheufele, M. Neuhaus, R. Nickel, F. Yakhov, K. Kummer, N. Brookes, L. Shen, G. L. Dakovski, N. J. Ghimire, S. Geprags, and M. F. Kling, Chiral altermagnon in MnTe, arXiv preprint arXiv:2501.17380 (2025).
- [43] N. Biniskos, M. dos Santos Dias, S. Agrestini, D. Sviták, K.-J. Zhou, J. Pospíšil, and Petr Čermák, Systematic mapping of altermagnetic magnons by resonant inelastic x-ray circular dichroism, arXiv preprint arXiv:2503.02533 (2025).
- [44] S. Bao, Z.-L. Gu, Y. Shangguan, Z. Huang, J. Liao, X. Zhao, B. Zhang, Z.-Y. Dong, W. Wang, R. Kajimoto, M. Nakamura, T. Fennell, S.-L. Yu, J.-X. Li, and J. Wen, Direct observation of topological magnon polarons in a multiferroic material, *Nat. Commun.* **14** (2023).
- [45] Y. Wei, Y. Tseng, H. Elnaggar, W. Zhang, T. C. Asmara, E. Paris, G. Domaine, V. N. Strocov, L. Testa, V. Favre, M. Di Luca, M. Banerjee, A. R. Wildes, F. M. F. de Groot, H. M. Rønnow, and T. Schmitt, Spin-orbital excitations encoding the magnetic phase transition in the van der waals antiferromagnet  $\text{FePS}_3$ , *npj Quantum Mater.* **10**, 61 (2025).
- [46] F. K. Lotgering, Paramagnetic susceptibilities of  $\text{Fe}^{2+}$  and  $\text{Ni}^{2+}$  ions at tetrahedral or octahedral sites of oxides, *J. Phys. Chem. Solids* **23**, 1153 (1962).
- [47] P. Strobel, Y. Le Page, and S. McAlister, Growth and physical properties of single crystals of  $\text{Fe}^{\text{II}}_2\text{Mo}^{\text{IV}}_3\text{O}_8$ , *J. Solid State Chem.* **42**, 242 (1982).
- [48] A. Singh, H. Y. Huang, Y. Y. Chu, C. Y. Hua, S. W. Lin, H. S. Fung, H. W. Shiu, J. Chang, J. H. Li, J. Okamoto, C. C. Chiu, C. H. Chang, W. B. Wu, S. Y. Perng, S. C. Chung, K. Y. Kao, S. C. Yeh, H. Y. Chao, J. H. Chen, D. J. Huang, and C. T. Chen, Development of the soft X-ray AGM-AGS RIXS beamline at the Taiwan photon source, *J. Synchrotron Radiat.* **28**, 977 (2021).
- [49] P. Blaha, K. Schwarz, G. Madsen, D. Kvasnicka, and J. Luitz, *WIEN2k, An Augmented Plane Wave + Local Orbitals Program for Calculating Crystal Properties (Karlheinz Schwarz, Techn. Universität Wien, Austria, 2001)*, ISBN 3-9501031-1-2.
- [50] A. A. Mostofi, J. R. Yates, G. Pizzi, Y.-S. Lee, I. Souza, D. Vanderbilt, and N. Marzari, An updated version of wannier90: A tool for obtaining maximally-localised wannier functions, *Comput. Phys. Commun.* **185**, 2309 (2014).



# Supplementary Information

## 1 Experimental data analysis

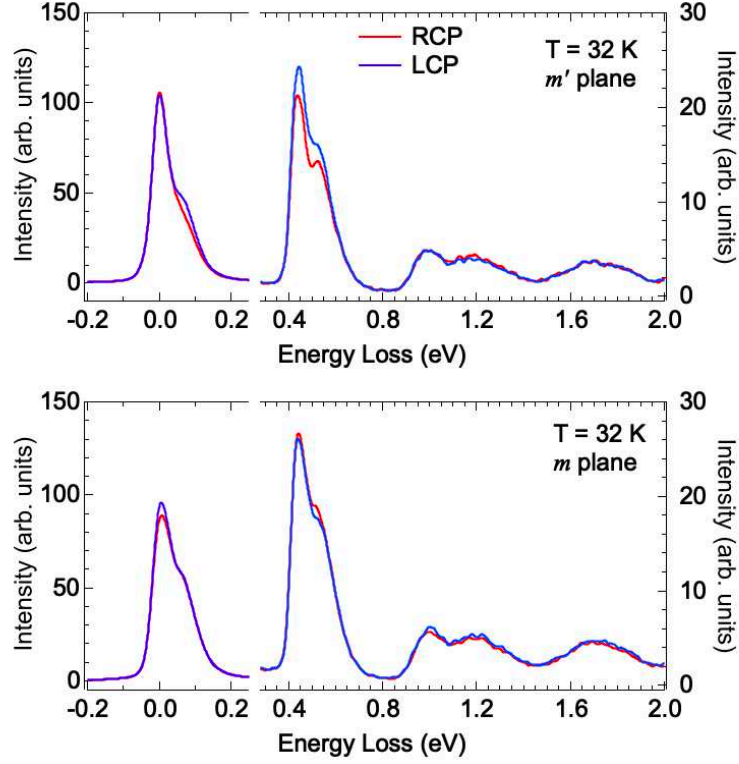


Figure S1: **Comparison of CD in RIXS of  $\text{Fe}_2\text{Mo}_3\text{O}_8$ .** Upper Panel: RIXS spectra measured with circularly polarized X-rays and with the scattering plane in the  $a^*c^*$  plane ( $m'$  symmetry plane) at 32 K, below the Néel temperature  $T_N = 60$  K. Red and blue curves, denoted by RCP and LCP, represent RIXS spectra excited with right- and left-handed circularly polarized incident X-rays, respectively. The RIXS data were recorded with momentum transfer  $\mathbf{Q} = (0.05, 0, 0.65)$ . Lower Panel: Corresponding RIXS spectra measured with the scattering plane in the  $ac$  plane ( $m$  symmetry plane) at 32 K.

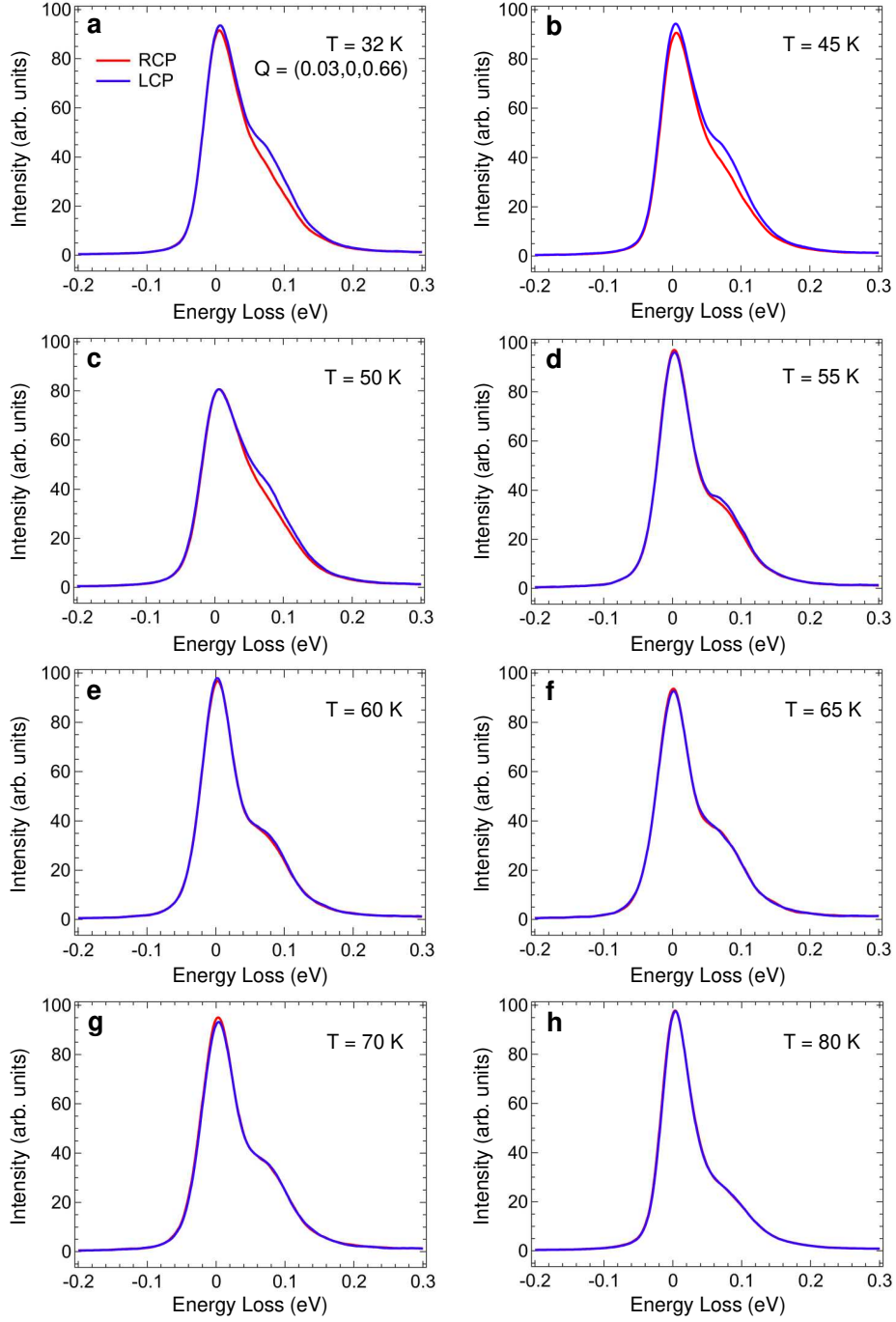


Figure S2: **a-h**, Temperature-dependent CD in the low-energy spin-orbital excitations of  $\text{Fe}_2\text{Mo}_3\text{O}_8$  measured across the  $T_N$  with circularly polarized X-rays at  $\mathbf{Q} = (0.03, 0, 0.66)$ . Red and blue curves, denoted by RCP and LCP, represent RIXS spectra excited with right- and left-circularly polarized incident X-rays, respectively.

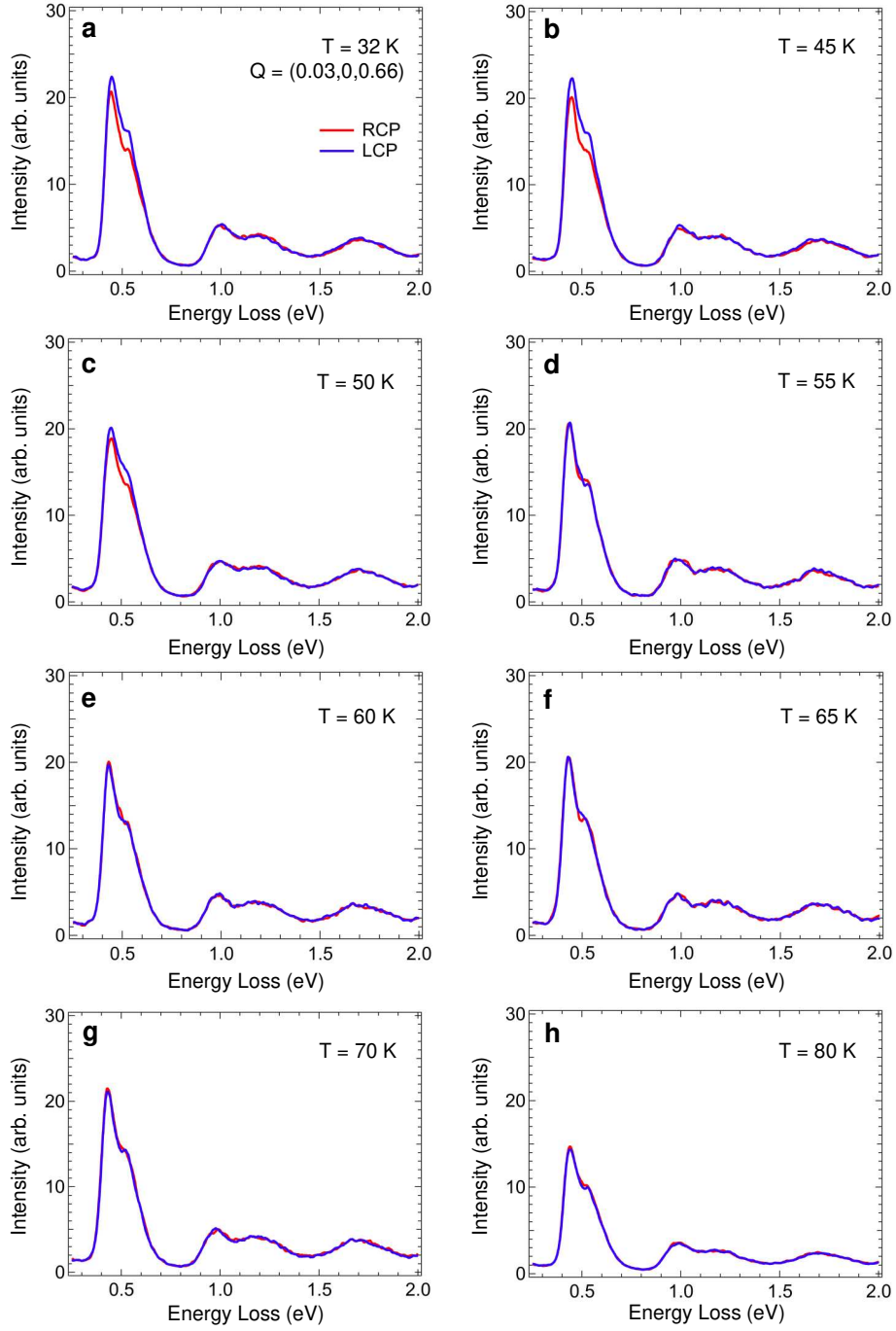


Figure S3: **a-h**, Temperature-dependent CD in the crystal-field excitations of  $\text{Fe}_2\text{Mo}_3\text{O}_8$  measured across the  $T_N$  with circularly polarized X-rays at  $\mathbf{Q} = (0.03, 0, 0.66)$ . Red and blue curves, denoted by RCP and LCP, represent RIXS spectra excited with right- and left-circularly polarized incident X-rays, respectively.

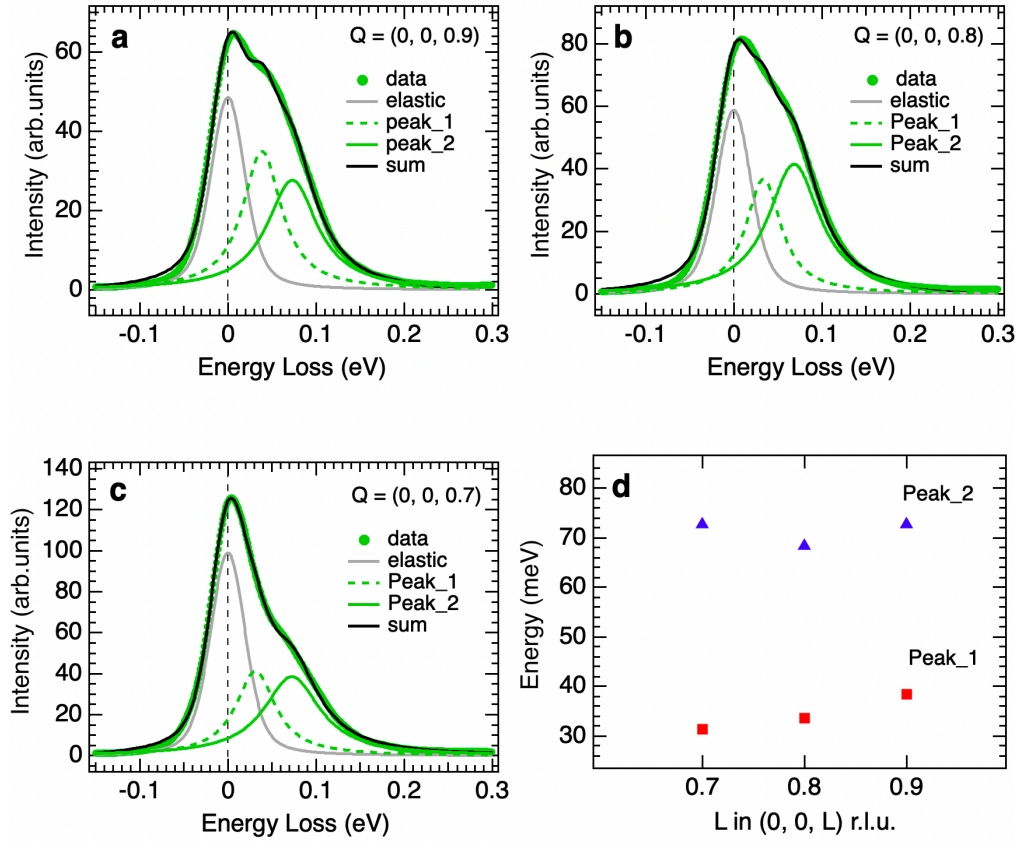


Figure S4: **Fitting results for the  $Q$ -dependent RIXS.** **a-c**, Momentum-dependent dispersion of spin-orbital excitations of  $\text{Fe}_2\text{Mo}_3\text{O}_8$  measured at  $Q = (0, 0, L)$  with right-circular polarized X-ray. The green solid circle indicates the experimental data, and the black solid line represents the sum of the fitting peaks. The fitted model consists of a Voigt profile (gray solid line) for the elastic peak and Lorentzian profiles for the spin-orbital excitations, represented by the green dotted and solid lines for peak 1 and peak 2, respectively. **d**, Dispersion of peak 1 (red square) and peak 2 (blue triangle) extracted from the fitting results.

## 2 RIXS simulation

Here we describe our RIXS simulation of  $\text{Fe}_2\text{Mo}_3\text{O}_8$  using an ionic model. We first construct two ionic models representing the quasi- $O_h$  and  $T_d$  sites, starting from density functional theory calculations. The derived parameters are then further optimized under three criteria ( $C1$ ,  $C2$ ,  $C3$ ) imposed by the present RIXS data shown in Fig. S5(a). Based on these optimized ionic models, we proceed with the simulation of the RIXS-CD of  $\text{Fe}_2\text{Mo}_3\text{O}_8$ .

- $C1$ . Both Fe sites adopt a divalent  $d^6$  configuration with well-localized  $d$  electrons. Therefore, we use the same interaction parameters for the  $3d$ – $3d$  (valence–valence) and  $2p$ – $3d$  (core–valence) Coulomb multiplet interactions at the two Fe sites. For the core–valence interaction, the Slater integrals are computed using atomic Hartree–Fock calculations, and the values are reduced to 70% of the bare values to account for the effect of higher configurations, which is a well-established empirical treatment for simulating core-level spectra at  $3d$  transition metal edges [1, 2, 3, 4, 5]. The  $3d$ – $3d$  interaction is parameterized by the Hund’s parameter  $J_H = (F_2 + F_4)/14$ , where  $F_2$  and  $F_4$  are Slater integrals. We set  $J_H = 0.75$  eV, which is a typical value for Fe-based oxides, and its validity is confirmed by the position of the  $dd$  features, as explained in criteria 3. The two Fe sites are distinguished by the crystal-field terms in the corresponding ionic Hamiltonian, which are determined straightforwardly from the experimental criteria 2 ( $T_d$  site) and 3 ( $O_h$  site) described below.
- $C2$ . The  $T_d$  site exhibits a distinct  $dd$  excitation (feature  $B$ ) around 0.4–0.5 eV, Fig. S5(a), corresponding to the  ${}^5T$  excitation (in the absence of the spin-orbit coupling). The excitation energy from the ground state ( ${}^5E$ ) to this excited state is determined by the crystal-field splitting  $\text{CF}_{T_d}$  between the  $t$  and  $e$  orbitals in the  $T_d$  crystal environment, which allows us to estimate its reasonable value as  $\text{CF}_{T_d}^{\text{opt}} = 0.49$  eV, see the energy diagram in Fig. S5(b). In the experimental data, feature  $B$  exhibits fine structure arising from the spin–orbit coupling ( $\xi_{3d}$ ) within the Fe  $3d$  shell. As shown in Fig. S5(c),  $\xi_{3d}^{\text{opt}} = 65$  meV yields a splitting reasonably consistent with the experimental data. We therefore adopt this value at both the  $O_h$  and  $T_d$  sites in simulating the RIXS-CD. This value is slightly larger than the one derived from atomic calculations ( $\xi_{3d}^{\text{atom}} = 52$  meV). The discrepancy may be related to hybridization with ligand or Mo sites, which is not explicitly treated within the present ionic models. Note that we have checked that the presence or absence of CD is irrelevant with varying the spin–orbit coupling constant within this scale.
- $C3$ . The  $O_h$  site exhibits multiple  $dd$  features, labeled  $C$ , with a pronounced peak at approximately 1.0 eV and an additional feature around 1.2 eV, indicated as  $C'$  in Fig. S5(a). In Fig. S5(d), we show the calculated energy diagram as a function of the crystal-field splitting  $\text{CF}_{O_h}$  between  $t_{2g}$  and  $e_g$ , where spin–orbit coupling within the Fe  $3d$  shell is neglected for clarity, as it is not essential for the optimization of the  $O_h$  site discussed below. As seen in the simulated energy profile, the  ${}^5E_g$ ,  ${}^3T_{1g}$ , and  ${}^1A_1$  states are nearly degenerate at 1.0 eV. For the high-spin ground state ( ${}^5T_2$ ), however, the  ${}^5E$  excitation exhibits a stronger RIXS intensity owing to a spin-conserving process, and thus serves as the dominant contribution to the 1.0 eV  $C$  feature, compared to the intermediate-spin excitation  ${}^3T_2$ . The RIXS intensity of  ${}^1A_1$  is negligibly weak, consistent with  $L_3$ -edge RIXS studies on similar  $d^6$  systems [6, 7]. The higher intermediate-spin excitation  ${}^3T_2$  gives rise to the feature around 1.2 eV. We stress that the excitation energy of the  ${}^5E$  state is exclusively determined by the crystal-field splitting within the model, irrespective of the  $J_H$  value, since it has the same high-spin character as the ground state. This allows us to set the optimal crystal-field splitting  $\text{CF}_{O_h}^{\text{opt}}$  to 0.95 eV. By contrast, the intermediate-spin states ( ${}^3T_1$ ,  ${}^3T_2$ ) depend on  $J_H$ , and only a narrow range around  $J_H = 0.75$  eV yields agreement between their energies and the experimental data.



(see Fig. S5e). Simultaneously, the simulated spectra adopting  $CF_{O_h}^{\text{opt}}$  and  $J_H = 0.75$  eV reproduce additional features in the range 1.6–2.0 eV. In the RIXS-CD simulations below, we include spin–orbit coupling with  $\xi_{3d}^{\text{opt}} = 65$  meV in the derived ionic model at the  $O_h$  site.

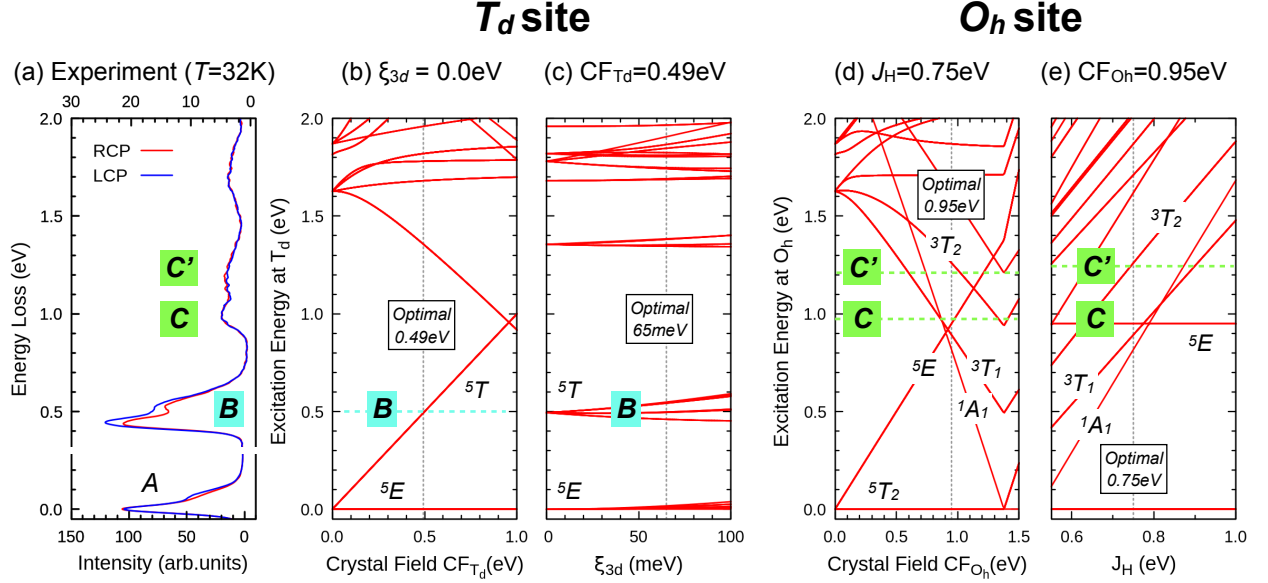


Figure S5: (a) Experimental Fe  $L_3$ -edge RIXS spectra measured with circularly polarized X-rays, reproduced from Fig. 2a in the main text. (b,c) Energy diagrams computed using the atomic model for the  $T_d$  site: (b) as a function of the crystal-field splitting  $CF_{T_d}$  (with spin–orbit coupling set to zero), and (c) as a function of the spin–orbit coupling  $\xi_{\text{soc}}$  for the optimal crystal-field splitting (0.49 eV). (d,e) Energy diagrams computed for the  $O_h$  site: (d) as a function of the crystal-field splitting  $CF_{O_h}$  and (e) as a function of the Hund’s coupling  $J_H$  for the optimal crystal-field splitting (0.95 eV), where spin–orbit coupling is neglected for clarity. In each panel, vertical bars indicate the optimal value reproducing the characteristic peak positions observed in the experimental RIXS data.

We note that the above optimization of the model relies only on the RIXS spectra, and the CD profile is not used in this process. We now proceed with the analysis of the RIXS-CD based on the optimized ionic model. To this end, we introduce an effective Weiss (exchange) field to represent the altermagnetic order in the lattice. As discussed in the main text, the ground-state manifold in the non-relativistic limit (i.e., without spin–orbit coupling) is  ${}^5T_2$  at the  $O_h$  site and  ${}^5E$  at the  $T_d$  site. Given the degrees of freedom in both spin and orbital angular momentum in the ground-state manifold, the effective field may in principle take a complex form, depending on both. In the present work, however, we do not attempt to derive the detailed form of the Weiss field, but instead restrict ourselves to the simplest form,  $H_{\text{Weiss}} = -\mathbf{S} \cdot \mathbf{B}_{\text{eff}}$ , assuming that it acts only in the spin space and that the field direction is parallel to the Néel vector. This simplified form reproduces the experimental data reasonably well, as shown in the main text and in the supplemental calculations below. Each  $O_h$  and  $T_d$  unit consists of two magnetic sublattices (i.e., four ion sites in total in the simulation). A staggered Weiss field is applied to the sublattices to simulate the antiferromagnetic arrangement of the magnetic moments [8, 9]. The total contributions from the  $O_h$  and  $T_d$  sites are then obtained by summing over the two magnetic sublattices within each unit.

Figures S6(a)e show the evolution of the low-energy spectrum with the Weiss field at the  $T_d$  and  $O_h$  sites, respectively. In Fig. S6(e), at the  $O_h$  site, spin–orbit coupling lifts the degeneracy of the  ${}^5T_2$  ground state, splitting it into  $J_{\text{eff}} = 1, 2, 3$ , as discussed in the main text. The Weiss field introduces a Zeeman effect in the  $J_{\text{eff}} = 1$  state, leading to a magnetic ground state. When

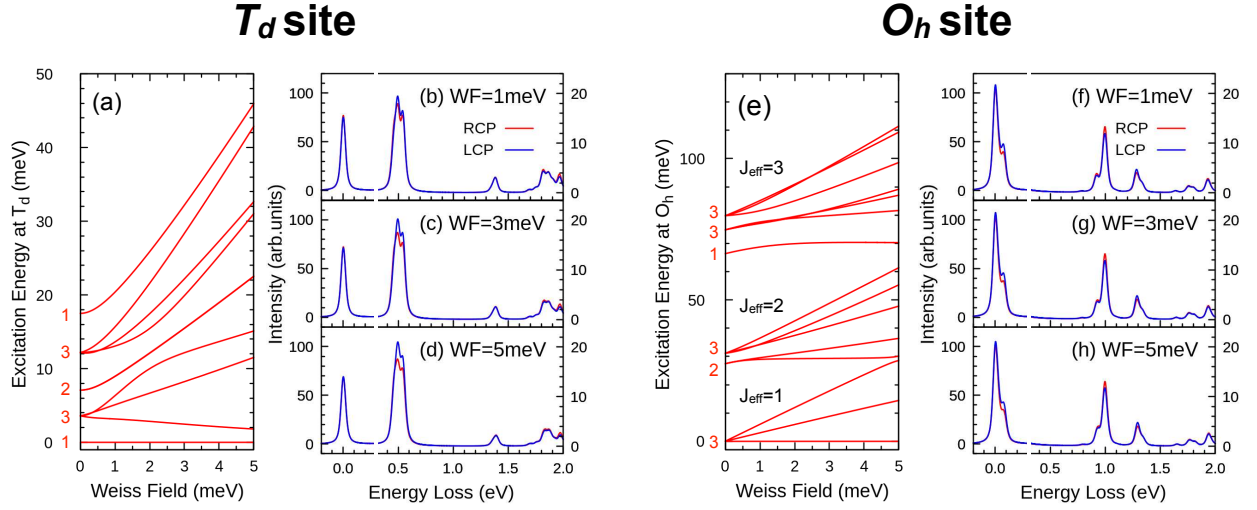


Figure S6: Evolution of the excitation energies with the altermagnetic Weiss (molecular) field at the  $T_d$  (left) and  $O_h$  (right) sites. The multiplicities of the excited states in the absence of the Weiss field are indicated in the panels. (b–d, f–h) Simulated RIXS-CD spectra for three selected amplitudes of the Weiss field (1, 3, and 5 meV) are shown for each Fe site.

a small distortion at the  $O_h$  site is taken into account, the spectrum is slightly modified, but the RIXS-CD remains unchanged, as we demonstrate below. In Fig. S6(a), at the  $T_d$  site, spin–orbit coupling stabilizes a singlet ground state out of the  $^5E$  manifold. However, when the Weiss field is turned on, both a sizable spin and an orbital angular momentum emerge in the ground state. For example, Weiss-field amplitudes of 1, 3, and 5 meV result in  $(S_c, L_c) = (1.29, 0.30)$ ,  $(1.67, 0.35)$ , and  $(1.80, 0.35)$ , respectively, where  $c$  denotes the crystallographic  $c$  direction. The sign of the moments is reversed between the magnetic sublattices, leading to compensation of the total magnetic moment. This behavior indicates that the magnetism at the  $T_d$  site is of the Van Vleck type. We have calculated the RIXS-CD from the ground state for selected amplitudes of the Weiss field. At around 3–5 meV, which appears to be a reasonable value for the studied system, we observe CD at features  $A$  and  $B$ . As explained in the main text, the former and latter originate from the  $O_h$ - and  $T_d$ -site contributions, respectively.

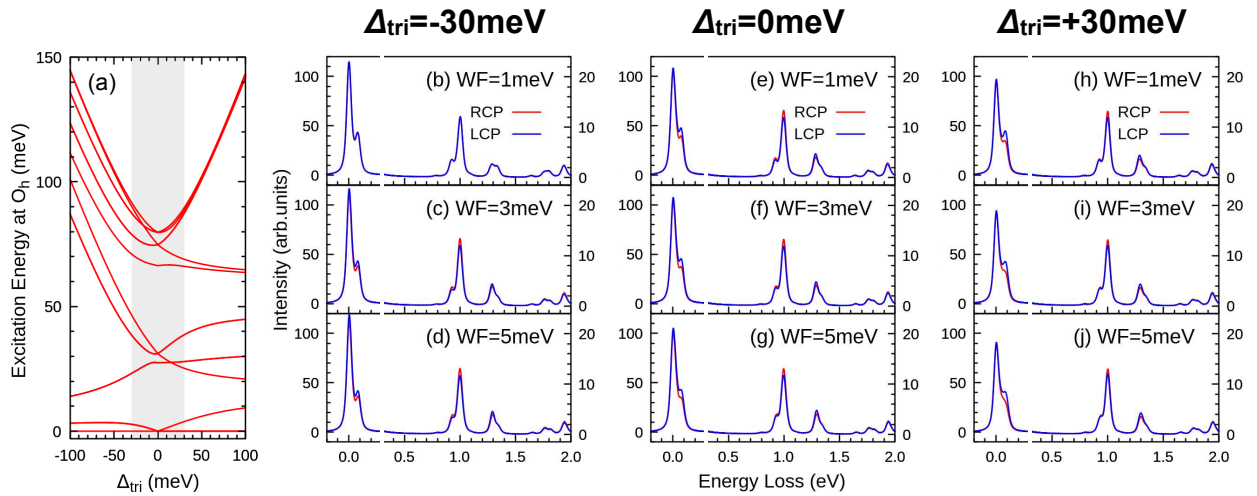


Figure S7: (a) Evolution of the excitation energies with the trigonal distortion  $\Delta_{tri}$  at the Fe  $O_h$  site. The simulated RIXS-CD spectra for three selected Weiss-field amplitudes (1, 3, and 5 meV) for  $\Delta_{tri} = -30, 0, 30$  meV are shown for comparison.

Finally, we comment on the effect of a distortion of the surrounding oxygens. At both the  $O_h$  and  $T_d$  sites, a small trigonal-like distortion splits the  $t$  level into a singlet ( $a_1$ ) and a doublet ( $e$ ), with the splitting denoted as  $\Delta_{\text{tri}}$  hereafter. As shown in Refs. [10, 11] and confirmed by our DFT simulations, the splitting at the  $T_d$  site is tiny. Furthermore the ground-state manifold at the  $T_d$  site is  ${}^5E$ , which is essentially unaffected to the  $\Delta_{\text{tri}}$  splitting. This justifies neglecting the splitting in our analysis. For the  $O_h$  site, however, the  ${}^5T$  ground-state degeneracy should be lifted by  $\Delta_{\text{tri}}$ , while both the magnitude and the sign of  $\Delta_{\text{tri}}$  appear to be difficult to determine [10, 11].

To provide support that the ambiguity in the distortion at the  $O_h$  site does not affect our analysis of RIXS-CD, we calculated the low-energy excitation spectrum in the range  $\Delta_{\text{tri}} = -100$  to 100 meV. Depending on the sign of  $\Delta_{\text{tri}}$ , a singlet (negative  $\Delta_{\text{tri}}$ ) or doublet (positive  $\Delta_{\text{tri}}$ ) ground state is realized. The present RIXS experiment, in Fig. S4(d), clarifies at least two spectral features centered around 35 meV and 70 meV, with minimal momentum dependence. The cases  $\Delta_{\text{tri}} = -30$  meV and 30 meV appear consistent with the experimental constraints, and the magnitude is also consistent with previous theoretical estimates. In Fig. S7, we present the calculated RIXS-CD spectra for  $\Delta_{\text{tri}} = -30, 0$ , and 30 meV for selected amplitudes of the Weiss field (WF). The evolution of the excitation spectrum with the Weiss field is shown in Fig. S7(a). We find that all cases yield very similar RIXS-CD spectra, with a peak at 70 meV, in agreement with the present RIXS-CD experiment. Therefore, we conclude that the effect of the small distortion is not relevant for the main discussion of the present work.

### 3 Spin-Orbit Coupling in the ${}^5T_{2g}$ Manifold

We will determine the relation between the atomic spin-orbit coupling constant  $\zeta$  and the effective spin-orbit coupling constant  $\zeta'$  in the  ${}^5T_{2g}$  manifold for a  $d^6$  ion in the octahedral crystal field, and then discuss the ground state of the  $T_{1g}$  manifold.

#### 1. Full Spin-Orbit Hamiltonian Expectation Value

The full atomic spin-orbit Hamiltonian is given by:

$$H_1 = \zeta \sum_i \mathbf{l}_i \cdot \mathbf{s}_i. \quad (1)$$

We consider a 6-electron configuration in the  $t_{2g}$  and  $e_g$  orbitals, representing the high-spin  $t_{2g}^4 e_g^2$  configuration. or the  $e_g$  level, both orbitals are filled with spin-up electrons. For the  $t_{2g}$  level, we fill all three  $t_{2g}$  orbitals with spin-up electrons and one with spin-down:

$$\uparrow_{xy}, \uparrow_{yz}, \uparrow_{zx}, \downarrow_{xy} \quad (2)$$

Let us denote the one-electron basis set from the  $t_{2g}$  level, which have an effective angular momentum  $l_{\text{eff}} = 1$  and spin  $s = \frac{1}{2}$  by  $|m_l, m_s\rangle$ , where  $m_l = \pm 1, 0$  and  $m_s = \pm \frac{1}{2}$ . The full spin-orbit Hamiltonian is:

$$H_1 = \zeta \sum_{i=1}^4 \mathbf{l}_i \cdot \mathbf{s}_i = \zeta \sum_{i=1}^4 (l_{i,z} s_{i,z} + \frac{1}{2} (l_{i,+} s_{i,-} + l_{i,-} s_{i,+})) \quad (3)$$

Since the basis states are eigenstates of  $l_z$  and  $s_z$ , only the  $l_z s_z$  terms contribute in this state; the off-diagonal terms vanish. We then have

$$\langle H_1 \rangle = \zeta \sum_{i=1}^4 \langle m_l^{(i)} m_s^{(i)} | l_z^{(i)} s_z^{(i)} | m_l^{(i)} m_s^{(i)} \rangle = \zeta \sum_{i=1}^4 m_l^{(i)} m_s^{(i)} \quad (4)$$

Considering the individual states explicitly:

$$\begin{aligned} (1) \quad & |1, \frac{1}{2}\rangle \Rightarrow m_l = +1, m_s = +\frac{1}{2} \Rightarrow m_l m_s = +\frac{1}{2} \\ (2) \quad & |0, \frac{1}{2}\rangle \Rightarrow m_l = 0, m_s = +\frac{1}{2} \Rightarrow m_l m_s = 0 \\ (3) \quad & |-1, \frac{1}{2}\rangle \Rightarrow m_l = -1, m_s = +\frac{1}{2} \Rightarrow m_l m_s = -\frac{1}{2} \\ (4) \quad & |-1, -\frac{1}{2}\rangle \Rightarrow m_l = -1, m_s = -\frac{1}{2} \Rightarrow m_l m_s = +\frac{1}{2} \end{aligned}$$

Summing all contributions:

$$\langle H_1 \rangle = \zeta \left( \frac{1}{2} + 0 - \frac{1}{2} + \frac{1}{2} \right) = \zeta \cdot \frac{1}{2} \quad (5)$$

That is,

$$\langle H_1 \rangle = \frac{\zeta}{2} \quad (6)$$

#### 2. Effective Hamiltonian in the ${}^5T_{2g}$ Manifold

In the  $t_{2g}$  manifold, the effective angular momentum is  $L_{\text{eff}} = 1$ , and the effective Hamiltonian becomes:

$$H_2 = \zeta' \mathbf{L}_{\text{eff}} \cdot \mathbf{S} \quad (7)$$

If we ignore the contributions of the two  $e_g$  electrons in the  ${}^5T_{2g}$  term, and use the identity

$$\mathbf{L}_{\text{eff}} \cdot \mathbf{S} = \frac{1}{2} [J_{\text{eff}}(J_{\text{eff}} + 1) - L_{\text{eff}}(L_{\text{eff}} + 1) - S(S + 1)], \quad (8)$$

the spin-orbit coupling (SOC) is

$$\mathbf{L}_{\text{eff}} \cdot \mathbf{S} = \frac{1}{2}(12 - 2 - 6) = 2 \Rightarrow \langle H_1 \rangle = 2\zeta', \quad (9)$$

for  $S = 2$ ,  $L_{\text{eff}} = 1$  and  $J = |L + S| = 3$ .

We now equate the two results and have

$$\langle H_1 \rangle = \langle H_2 \rangle \Rightarrow \frac{\zeta}{2} = 2\zeta' \Rightarrow \zeta' = \frac{\zeta}{4}. \quad (10)$$

The SOC splits the  ${}^5T_2$  state into triplet, quintet, and septet states with effective angular momentum  $J_{\text{eff}} = 1, 2$ , and  $3$ . Using Eqs. 7 and 8, one can obtain the energy splittings between  $J_{\text{eff}} = 1$  and  $2$ , and between  $2$  and  $3$ ; they are  $\frac{1}{2}\zeta$  and  $\frac{3}{4}\zeta$ , respectively.

### 3. Spin-Orbit-Coupled Ground State

The lowest spin-orbital state  $T_{1g}$  of the  ${}^5T_{2g}$  manifold can also be regarded as an  $J_{\text{eff}} = 1$  state and its eigenfunctions  $|J, J_z\rangle$ , where  $z$  is taken parallel to the crystallographic  $c$  axis of  $\text{Fe}_2\text{Mo}_3\text{O}_8$ , are given by:

$$\begin{aligned} |J_{\text{eff}} = 1, J_{\text{eff},z} = 1\rangle &= \sqrt{\frac{1}{10}}|1, 0\rangle - \sqrt{\frac{3}{10}}|0, 1\rangle + \sqrt{\frac{3}{5}}|-1, 2\rangle, \\ |J_{\text{eff}} = 1, J_{\text{eff},z} = 0\rangle &= \sqrt{\frac{3}{10}}|1, -1\rangle - \sqrt{\frac{2}{5}}|0, 0\rangle + \sqrt{\frac{3}{10}}|-1, 1\rangle, \\ |J_{\text{eff}} = 1, J_{\text{eff},z} = -1\rangle &= \sqrt{\frac{3}{5}}|1, -2\rangle - \sqrt{\frac{3}{10}}|0, -1\rangle + \sqrt{\frac{1}{10}}|-1, 0\rangle, \end{aligned} \quad (11)$$

where  $|L_{\text{eff},z}, S_z\rangle \equiv |L_{\text{eff},z}\rangle|S_z\rangle$ . The  $z$ -components of the magnetic moments are  $-\frac{5}{2}\mu_B$ ,  $0$ , and  $\frac{5}{2}\mu_B$ , respectively. The magnetic moment is given by  $\boldsymbol{\mu} = -g\mu_B\mathbf{J}$ . For  $J_{\text{eff}} = 1$ ,  $L_{\text{eff}} = 1$ , and  $S = 2$ , the Landé  $g$ -factor is  $g = \frac{5}{2}$ . Therefore, the  $z$ -components of the magnetic moment for  $J_z = 1, 0$ , and  $-1$  are  $-\frac{5}{2}\mu_B$ ,  $0$ , and  $\frac{5}{2}\mu_B$ , respectively. The magnitude of the magnetic moment  $\frac{5}{2}\mu_B$  is smaller than the  $S = 2$  spin-only value of  $4\mu_B$  due to the anti-parallel contributions of the orbital magnetic moment.

## References

- [1] Atsushi Hariki, Takayuki Uozumi, and Jan Kuneš. LDA+DMFT approach to core-level spectroscopy: Application to  $3d$  transition metal compounds. *Phys. Rev. B*, 96:045111, Jul 2017.
- [2] Masahiko Matsubara, Takayuki Uozumi, Akio Kotani, and Jean Claude Parlebas. Charge transfer excitation in resonant x-ray emission spectroscopy of NiO. *J. Phys. Soc. Jpn.*, 74(7):2052–2060, 2005.
- [3] Jack Sugar. Potential-barrier effects in photoabsorption. ii. interpretation of photoabsorption resonances in lanthanide metals at the  $4d$ -electron threshold. *Phys. Rev. B*, 5:1785–1792, Mar 1972.



- [4] Arata Tanaka and Takeo Jo. Temperature dependence of 2p-core x-ray absorption spectra in 3d transition-metal compounds. *J. Phys. Soc. Jpn.*, 61(6):2040–2047, 1992.
- [5] F. M. F. de Groot, J. C. Fuggle, B. T. Thole, and G. A. Sawatzky. 2p x-ray absorption of 3d transition-metal compounds: An atomic multiplet description including the crystal field. *Phys. Rev. B*, 42:5459–5468, Sep 1990.
- [6] Ru-Pan Wang, Atsushi Hariki, Andrii Sotnikov, Federica Frati, Jun Okamoto, Hsiao-Yu Huang, Amol Singh, Di-Jing Huang, Keisuke Tomiyasu, Chao-Hung Du, Jan Kuneš, and Frank M. F. de Groot. Excitonic dispersion of the intermediate spin state in  $\text{LaCoO}_3$  revealed by resonant inelastic x-ray scattering. *Phys. Rev. B*, 98:035149, Jul 2018.
- [7] Atsushi Hariki, Ru-Pan Wang, Andrii Sotnikov, Keisuke Tomiyasu, Davide Betto, Nicholas B. Brookes, Yohei Uemura, Mahnaz Ghiasi, Frank M. F. de Groot, and Jan Kuneš. Damping of spinful excitons in  $\text{LaCoO}_3$  by thermal fluctuations: Theory and experiment. *Phys. Rev. B*, 101:245162, Jun 2020.
- [8] M. Furo, A. Hariki, and J. Kuneš. Theory of circular dichroism in resonant inelastic x-ray scattering. *arXiv preprint arXiv:2508.04388*, 2025.
- [9] A. Hariki, A. Dal Din, O. J. Amin, T. Yamaguchi, A. Badura, D. Kriegner, K. W. Edmonds, R. P. Champion, P. Wadley, D. Backes, L. S. I. Veiga, S. S. Dhesi, G. Springholz, L. Šmejkal, K. Výborný, T. Jungwirth, and J. Kuneš. X-Ray Magnetic Circular Dichroism in Altermagnetic  $\alpha\text{-MnTe}$ . *Phys. Rev. Lett.*, 132:176701, Apr 2024.
- [10] IV Solovyev and SV Streltsov. Microscopic toy model for magnetoelectric effect in polar  $\text{Fe}_2\text{Mo}_3\text{O}_8$ . *Phys. Rev. Mater.*, 3(11):114402, 2019.
- [11] S. Reschke, A. A. Tsirlin, N. Khan, L. Prodan, V. Tsurkan, I. Kézsmárki, and J. Deisenhofer. Structure, phonons, and orbital degrees of freedom in  $\text{Fe}_2\text{Mo}_3\text{O}_8$ . *Phys. Rev. B*, 102:094307, Sep 2020.